

Supplementary Information

Tuning Reduction Conditions to Understand and Control Ni Exsolution from



Willis O'Leary, Livia Giordano, Jennifer L.M. Rupp

Contents

S.1. Characterization of exsolution on fracture surfaces using Fiji	3
S.2. Design of reducing atmospheres using thermodynamic calculations.....	4
S.3. Theory of the exsolution driving force	8
S.4. Derivation of ΔG_{segDFT} and ΔG_{redDFT} as continuous functions of $\Delta\mu\text{O}$	9
S.5. Analysis based on DFT calculations on a large slab model	10
References.....	12

Table S1. Partial review of works studying influence of reduction conditions on exsolution of metal nanoparticles from perovskites.

Stoichiometry	Reduction atmosphere(s) ^a	Reduction temperature	Observations on nanoparticle dimensions	Ref.
La _{0.5} Sr _{0.5} Fe _{0.8} Ni _{0.1} Nb _{0.1} O _{3-δ}	3% H ₂ O in H ₂	300-900 °C	As temperature increases: <ul style="list-style-type: none"> • Radius constant, then increases past 700 °C • Density increases, peaks at 800 °C, then decreases 	1
	5% H ₂ in Ar	700-900 °C	As temperature increases: <ul style="list-style-type: none"> • Radius increases • Particle density slightly increases 	
Nd _{0.6} Ca _{0.4} Fe _{0.9} Co _{0.1} O _{3-δ}	50% Ar, 25% CO ₂ , 25% H ₂	Ramp up and down between 300 °C and 700 °C	As more H ₂ is introduced: <ul style="list-style-type: none"> • Radius increases • Density increases 	2
	50% Ar, ~3% H ₂ , ~47% CO ₂			
La _{0.2} Sr _{0.7} Ti _{0.9} Ni _{0.1} O _{3-δ}	5% H ₂ in Ar	800-1000 °C	As temperature increases: <ul style="list-style-type: none"> • Radius increases • Density decreases 	3
La _{0.43} Ca _{0.37} Rh _{0.01} Ti _{0.99} O _{3-δ}	5% H ₂ in He	500-1000 °C	As temperature increases: <ul style="list-style-type: none"> • Particle radius increases • Density first increases, peaks at 700 °C, then decreases 	4
LaAl _{0.8} Ni _{0.2} O _{3-δ}	5% H ₂ in N ₂	650-750 °C	As temperature increases: <ul style="list-style-type: none"> • Radius increases 	5
La _{0.5} Ca _{0.4} Ni _{0.2} Ti _{0.8} O _{3-δ}	H ₂	700-1000 °C	As temperature increases: <ul style="list-style-type: none"> • Radius increases • Density decreases 	6
La _{0.43} Ca _{0.37} Rh _{0.06} Ti _{0.94} O _{3-δ}	5% H ₂ in N ₂	600-900 °C	As temperature increases: <ul style="list-style-type: none"> • Radius increases • Density decreases 	7
La _{0.4} Sr _{0.4} Sc _{0.9} Ni _{0.1} O _{3-δ}	H ₂	900 °C	As more H ₂ is introduced: <ul style="list-style-type: none"> • Radius increases 	8
	20% H ₂	900 °C		
La _{0.9} Fe _{0.9} Ni _{0.05} Co _{0.05} O _{3-δ} LaFe _{0.9} Ni _{0.05} Co _{0.05} O _{3-δ}	5% H ₂ in He	800-950 °C	As temperature increases: <ul style="list-style-type: none"> • Radius increases 	9
La _{0.3} Sr _{0.7} Cr _{0.3} Fe _{0.6} Co _{0.1} O _{3-δ}	5% H ₂ in Ar	700-800 °C	As temperature increases: <ul style="list-style-type: none"> • Radius increases 	10

			<ul style="list-style-type: none"> • Density decreases 	
$\text{Sr}_{0.98}\text{Ti}_{0.95}\text{Co}_{0.05}\text{O}_{3-\delta}$	$\text{H}_2\text{O}, \text{H}_2, \text{Ar}$ ($p_{\text{O}_2} = 10^{-20}, 10^{-23}, 10^{-26}$ atm)	700-800 °C	<ul style="list-style-type: none"> • Density decreases As temperature increases: <ul style="list-style-type: none"> • Radius decreases • Density increases As p_{O_2} decreases: <ul style="list-style-type: none"> • Radius decreases • Density increases 	11
	$p_{\text{O}_2}=10^{-28}$	450-550 °C	As temperature increases: <ul style="list-style-type: none"> • Particle radius decreases • Density increases 	

^a Reported gas percentages are in units of vol% unless noted.

S.1. Characterization of exsolution on fracture surfaces using Fiji

The radii and densities of nanoparticles exsolved on fracture surfaces were analyzed using Fiji^{12,13}, a distribution of ImageJ, using the methodology shown in **Figure S1**. First, contrast and brightness were adjusted so that nanoparticles appeared maximally bright against the perovskite backbone. A brightness threshold was then applied to mark the nanoparticle areas. Irrelevant bright regions (for example edges) were manually removed as appropriate. ImageJ’s “analyze particles” function was used to measure all nanoparticle areas. Assuming nanoparticles were spherical, nanoparticle radii was calculated as:

$$\text{Radius} = \sqrt{\text{Area}/\pi}$$

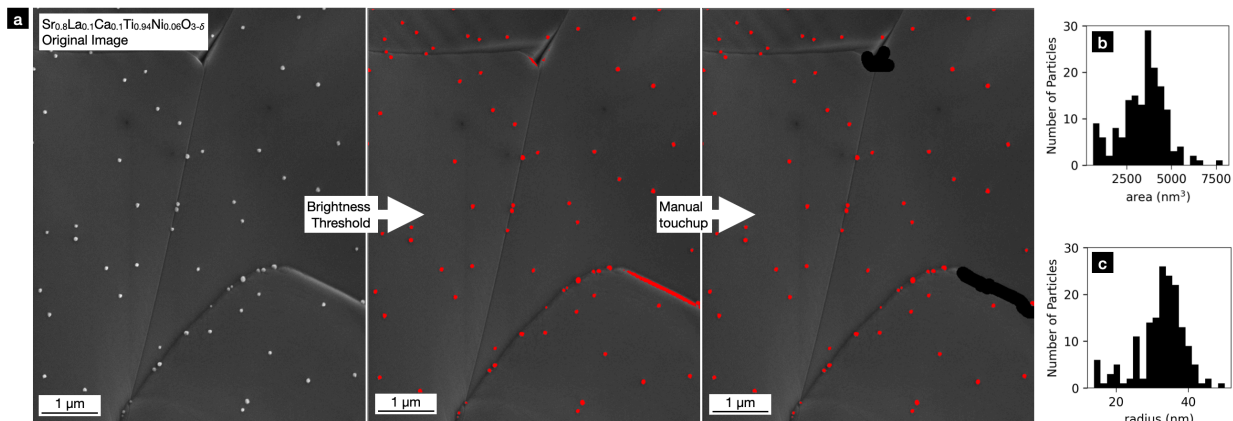


Figure S1. (a) Image analysis methodology used to measure nanoparticle radii and densities on fracture surfaces. First, a simple brightness threshold was applied to an image from SEM (red). Irrelevant bright surface features were manually removed. ImageJ’s automatic particle analysis routine was used to measure the areas of all marked nanoparticles. (b) Example histogram of nanoparticle areas generated from the image analysis. (c) Example histogram of particle radii calculated assuming spherical nanoparticles.

Nanoparticle density for a particular image was determined by dividing the number of nanoparticles by the area of the image.

This methodology could be easily applied to fracture surfaces. However, this methodology could not be applied to the native surfaces, as native surface's exhibited numerous bright artifacts which were tedious to remove manually. In the future, more advanced image processing could be applied to this task.

S.2. Design of reducing atmospheres using thermodynamic calculations

The reducing power of an atmosphere is typically quantified by oxygen partial pressure (p_{O_2}) or oxygen chemical potential (μ_O). In our case, it was most convenient to use the oxygen chemical potential, as exsolution energetics (derived via DFT, for example) are explicitly dependent on this quantity.

For each temperature, we chose the composition of the reduction atmospheres to evenly sample the same range of oxygen chemical potentials. We estimated the oxygen chemical potential of a given atmosphere with thermodynamic calculations, assuming equilibrium in the gas phase. We denoted oxygen chemical potential as $\Delta\mu_O$, defined as

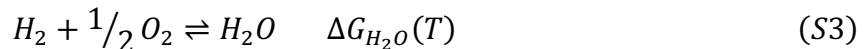
$$\Delta\mu_O(T, p_{O_2}) \approx \frac{(H_{\text{tab}}(T) - H_{\text{tab}}(0 \text{ K})) - TS_{\text{tab}}(T) + k_B T \log(p_{O_2})}{2} \quad (S1)$$

$H_{\text{tab}}(T)$ and $S_{\text{tab}}(T)$ define the enthalpy and entropy of O_2 in the gas phase and are tabulated in the JANAF¹⁴ tables. An ideal gas term takes p_{O_2} into account. In our DFT calculations, we used an re-referenced oxygen chemical potential:

$$\mu_{O,DFT} = \Delta\mu_O + \frac{E_{O_2,DFT} + E_{ZPE}}{2} \quad (S2)$$

$E_{O_2,DFT} = -9.87$ eV is the DFT energy for an isolated O_2 molecule. A zero-point energy correction $E_{ZPE} = 0.101$ eV is included.

We calculated p_{O_2} for a given H_2/Ar atmosphere with thermodynamic calculations. In a mixture of H_2 and Ar , p_{O_2} is dictated by the chemical equilibrium



where $\Delta G_{H_2O}(T)$ is the free energy of this reaction or, equivalently, the formation energy of water as tabulated in the JANAF¹⁴ tables. The equilibrium expression for this reaction at ambient pressure reads

$$\frac{p_{H_2O}}{p_{H_2} p_{O_2}^{0.5}} = \exp\left(-\frac{\Delta G_{H_2O}(T)}{kT}\right) \quad (S4)$$

In the furnace, we assumed a large and constant p_{H_2} (determined by the mass flow controllers). We also assumed a constant p_{H_2O} . Solving for p_{O_2} yields the expression:

$$\log p_{O_2} = 2\left(\frac{\Delta G_{H_2O}(T)}{kT} + \log(p_{H_2O}) - \log(p_{H_2})\right) \quad (S5)$$

We initially designing the reducing atmospheres under the assumption that all H₂O in the system came from impurities in the inlet gas stream. However, we believe such an assumption underestimates the amount of moisture in the system, which can enter through various leaks in the experimental apparatus.

Therefore, we repeated the calculations, this time assuming a small, constant p_{H_2O} . In a considerably more complex experimental setup containing longer lengths of tubing and a greater number of fittings and valves, we were able to achieve an atmosphere containing 0.003 % H₂O as measured by a Raman gas analyzer. We therefore believe that $p_{H_2O} = 3 \times 10^{-5}$ is a conservative estimate of the amount of moisture in our experimental setup at steady state. Under this assumption, we found that our $\Delta\mu_O$'s were 0.2 eV larger but covered an adequately consistent range across all temperatures (**Figure S2**). Assuming p_{H_2O} is any fixed value below 3×10^{-5} will shift all $\Delta\mu_O$'s by a fixed, negative number between 0 and -0.2 eV, again resulting in a consistent range across all temperatures.

Here, we must emphasize that the relationship between the reported values of $\Delta\mu_O$ and the conditions in which nucleation occur is not straightforward. More specifically, our hypothesis of burst nucleation of exsolution nanoparticles calls into question whether the assumption of steady-state gas-phase equilibrium holds during nucleation:

- 1) Burst nucleation occurs at the beginning of the reducing treatment; once H₂ is introduced into the Ar gas stream, it will take several minutes for the atmosphere within the furnace to reach steady state.
- 2) Upon reduction, a perovskite will release a substantial amount of oxygen, increasing the near-surface $\Delta\mu_O$. In our samples, oxygen release may be the result of both reduction of the SrTiO₃ host lattice (generating oxygen vacancies and Ti³⁺) or exsolution of Ni nanoparticles in the bulk¹⁵. Originally, we assumed that the continuous flow of reducing

gas would quickly negate this effect. However, if nucleation is indeed near-instantaneous upon exposure to reducing gas, as our work suggests, then this effect could be substantial. Therefore, our reported values for $\Delta\mu_O$ are ultimately nominal values. Since we performed these experiments in a single setup, use of these nominal values is acceptable. However, the hypothesis of burst nucleation suggests that reproduction of experimental exsolution studies between different groups could be extremely challenging.

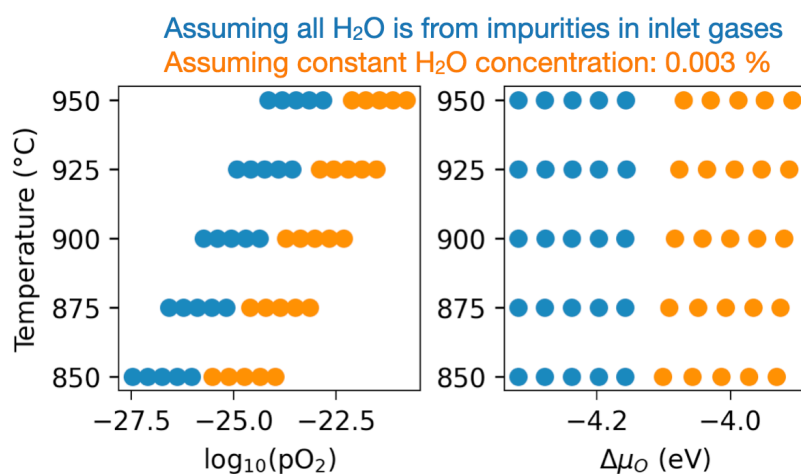


Figure S2. Exsolution temperatures, oxygen partial pressures, and oxygen chemical potentials accessed in this study as estimated by thermodynamic calculations. Two different assumptions of the water partial pressure were considered.

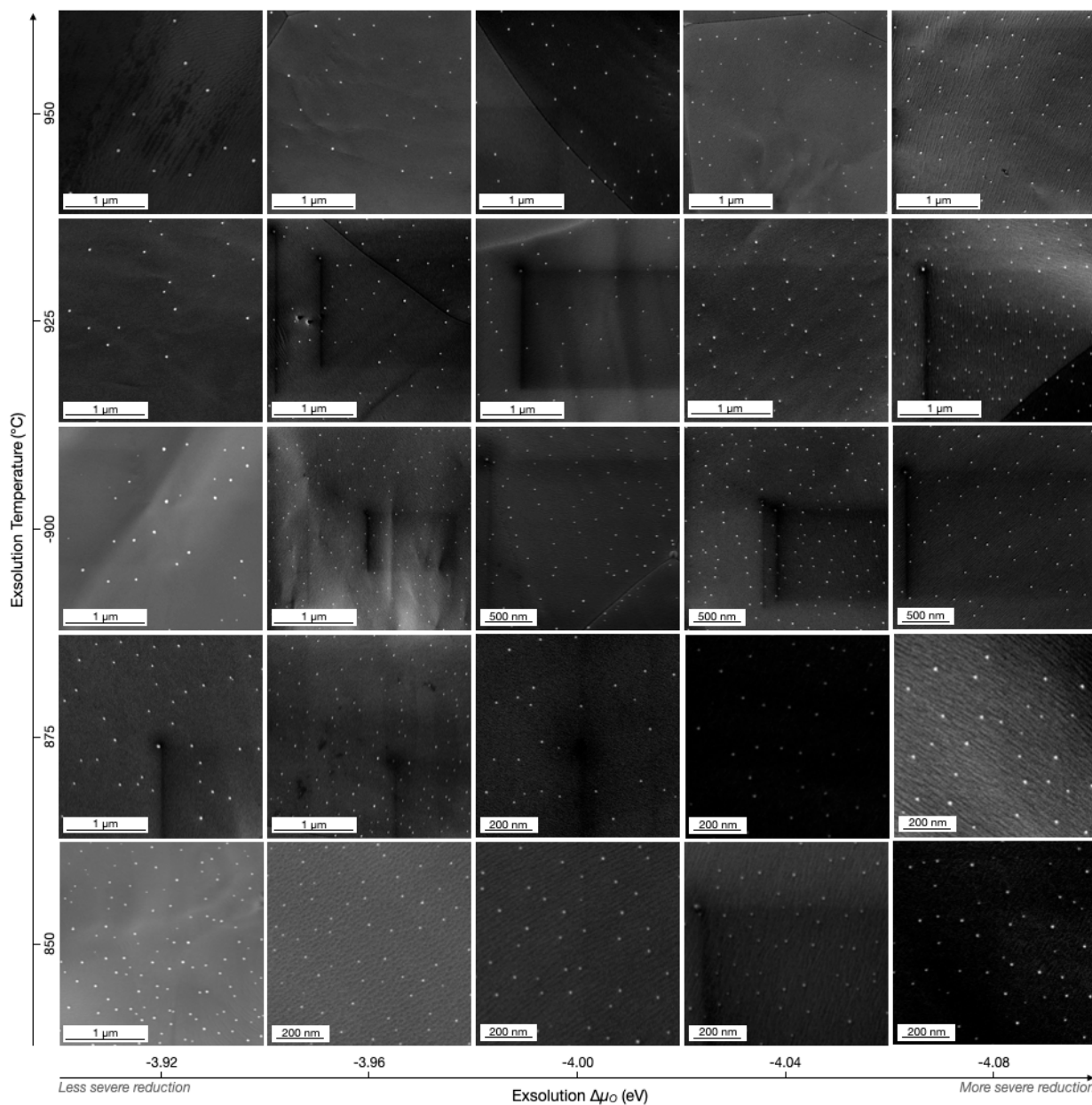


Figure S3. Representative SEM images of fracture surfaces after exsolution at various temperatures and oxygen chemical potentials. A wide range of nanoparticle sizes and surface densities were accessible.

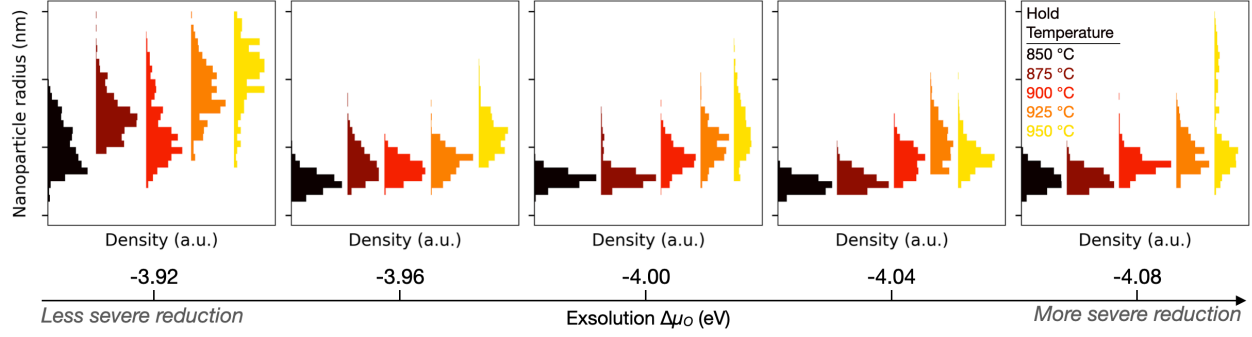
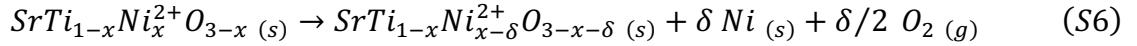


Figure S4. Nanoparticle radius histograms for samples treated under various temperatures and oxygen chemical potentials.

S.3. Theory of the exsolution driving force

We consider the hypothetical chemical equation of exsolution of Ni given by



This is derived from principles of charge neutrality. Ni is lost from the lattice and incorporated into metallic nanoparticles, leaving behind vacancies on the perovskite B-site. These must be neutralized by generation of oxygen vacancies. The driving force of this reaction $\Delta G(T, p_{\text{O}_2})$ is therefore given by:

$$\Delta G(T, p_{\text{O}_2}) = \delta \Delta\mu_{\text{Ni}}(T) + \delta\Delta\mu_{\text{O}}(p_{\text{O}_2}, T) + (\text{Perovskite/Nanoparticle Terms}) \quad (\text{S7})$$

Here, we wrap the terms related to the perovskite, nanoparticles, and their interfaces into a single term. $\Delta\mu_{\text{O}}$ is defined in Equation (S1). $\Delta\mu_{\text{Ni}}$ is defined as

$$\Delta\mu_{\text{Ni}} = (H_{\text{tab}}(T) - H_{\text{tab}}(0 \text{ K})) - TS_{\text{tab}}(T) \quad (\text{S8})$$

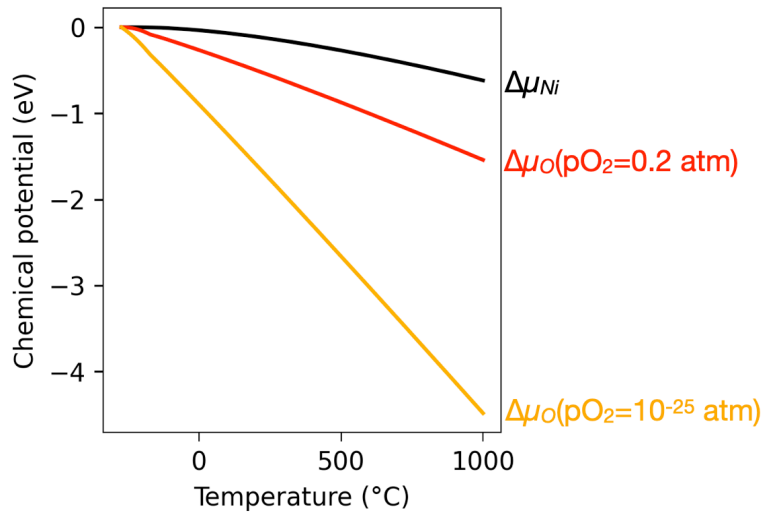


Figure S5. Chemical potentials of Ni and O versus temperature.

where $H_{\text{tab}}(T)$ and $S_{\text{tab}}(T)$ define the enthalpy and entropy of FCC Ni as tabulated in the JANAF¹⁴ tables. Both $\Delta\mu_{\text{Ni}}$ and $\Delta\mu_{\text{O}}$ are dependent on temperature, while $\Delta\mu_{\text{O}}$ is dependent on p_{O_2} as well (**Figure S5**).

In our experiments, we observed a roughly constant exsolution extent (volume of nanoparticles per surface area of perovskite). This may imply that the exsolution driving force is relatively constant over the small ranges of $\Delta\mu_{\text{O}}$ and temperature considered in this study. This is reasonable, as a) $\Delta\mu_{\text{Ni}}$ has weak dependence on temperature and b) only a small $\Delta\mu_{\text{O}}$ range was accessed in the experiments.

S.4. Derivation of $\Delta G_{\text{seg}}^{\text{DFT}}$ and $\Delta G_{\text{red}}^{\text{DFT}}$ as continuous functions of $\Delta\mu_{\text{O}}$

As discussed in the main text, we defined $\Delta G_{\text{seg}}^{\text{DFT}}$ and $\Delta G_{\text{red}}^{\text{DFT}}$ as continuous functions of $\Delta\mu_{\text{O}}$ by constructing composite functions,

$$\Delta G_{\text{seg}}^{\text{DFT}}(\Delta\mu_{\text{O}}) = \Delta G_{\text{seg}}^{\text{DFT}}(x(\Delta\mu_{\text{O}})) \quad (\text{S9})$$

$$\Delta G_{\text{red}}^{\text{DFT}}(\Delta\mu_{\text{O}}) = \Delta G_{\text{red}}^{\text{DFT}}(x(\Delta\mu_{\text{O}}), \Delta\mu_{\text{O}}) \quad (\text{S10})$$

where x is the surface oxygen stoichiometry of the DFT model (SrTiO_x). $\Delta G_{\text{seg}}^{\text{DFT}}(x)$ and $\Delta G_{\text{red}}^{\text{DFT}}(x)$ were defined as the linear interpolations shown in **Figure 6c**. A linear interpolation ensured consistency with our previous work, in which identical linear interpolations were essential when modelling exsolution in La-containing compositions. Here, due to the extra charge introduced by La^{3+} on a Sr^{2+} site, the small slab model could not capture the most stable O termination. We showed that using the small model one could estimate $\Delta G_{\text{seg}}^{\text{DFT}}$ and $\Delta G_{\text{red}}^{\text{DFT}}$ for this inaccessible termination through these same linear interpolations¹⁶.

We also derived a continuous function giving the equilibrium oxygen surface stoichiometry as a function of oxygen chemical potential, $x(\Delta\mu_{\text{O}})$. Consistent with our previous work, we based these calculations on slabs in which Ni was in the third layer. We first calculated the energies of the various O terminations. For a given x , we then defined the surface O removal energy $E_{-\text{O}}(x)$ as

$$E_{-\text{O}}(x) = \frac{E_{\text{slab}}(x + \delta) - E_{\text{slab}}(x - \delta)}{2\delta} 2\delta \quad (\text{S11})$$

The size of the slab model dictated which δ 's were accessible and therefore which x 's could be calculated. After determining O surface removal energies for these accessible x 's, we used linear

interpolations to derive a continuous function $E_{-o}(x)$. $x(\Delta\mu_o)$ is simply defined using the function inverse:

$$x(\Delta\mu_o) = E_{-o}^{-1}(-\Delta\mu_o) \quad (\text{S12})$$

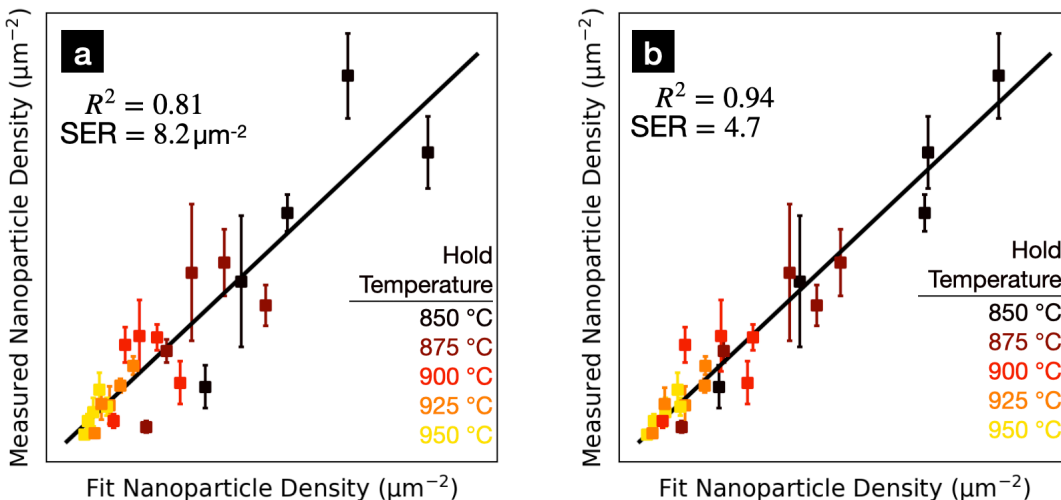


Figure S6. Fit results of our semiempirical model for nanoparticle density (a) including and (b) excluding explicit, linear dependence of the surface reduction rate on p_{H_2} . Excluding the dependence on p_{H_2} resulted in a superior fit to experimental data.

S.5. Analysis based on DFT calculations on a large slab model

As mentioned in the previous section, surface O removal energies $E_{-o}(x)$ were determined in the main text based on a small, ~ 50 atom slab model. To test dependence of our results on the size of the slab model, we derived $E_{-o}(x)$ based on a larger, ~ 100 atom slab model as well. This model was built by doubling the existing slab model in one direction (**Figure S7a**). Oxygen terminations for this model were built using the oxygen terminations used in the small models. Since the model was twice as large, Equation (S11) could be evaluated for different x 's.

	Empirical	DFT (single slab)	DFT (double slab)
$d\Delta G_{seg}/d\Delta\mu_O$	3.13	4.31	2.12
$d\Delta G_{red}/d\Delta\mu_O$	-	-0.87	0.22
$d(\Delta G_{red} - \Delta G_{grow})/d\Delta\mu_O$	-1.32	-	-

Table S2. Dependence of exsolution energetics on oxygen chemical potential, as determined from our semiempirical model and DFT calculations. Dependences of DFT-derived energies based on the more consistent single slab calculations were in better agreement with experiment, while the energies calculated using the larger slabs disagreed more.

The surface O removal energies calculated for the large, “double” slab are compared against those calculated in the main text with the “single” slab in **Figure S7b**. There was reasonable agreement between the double slab and single slab calculations, at least considering the different sizes of these models. However, the interpolations did differ substantially, meaning that dE_{-O}/dx was substantially different when calculated using the double slab model. This had significant effects on the calculated $\Delta G_{seg}^{DFT}(x)$ and $\Delta G_{red}^{DFT}(x)$ (**Figure S7c**). In particular, the slopes, tabulated in **Table S2**, no longer agreed well with the experimentally determined energies. This change can be traced to the different $x(\Delta\mu_O)$ derived from the larger model. The sensitivity

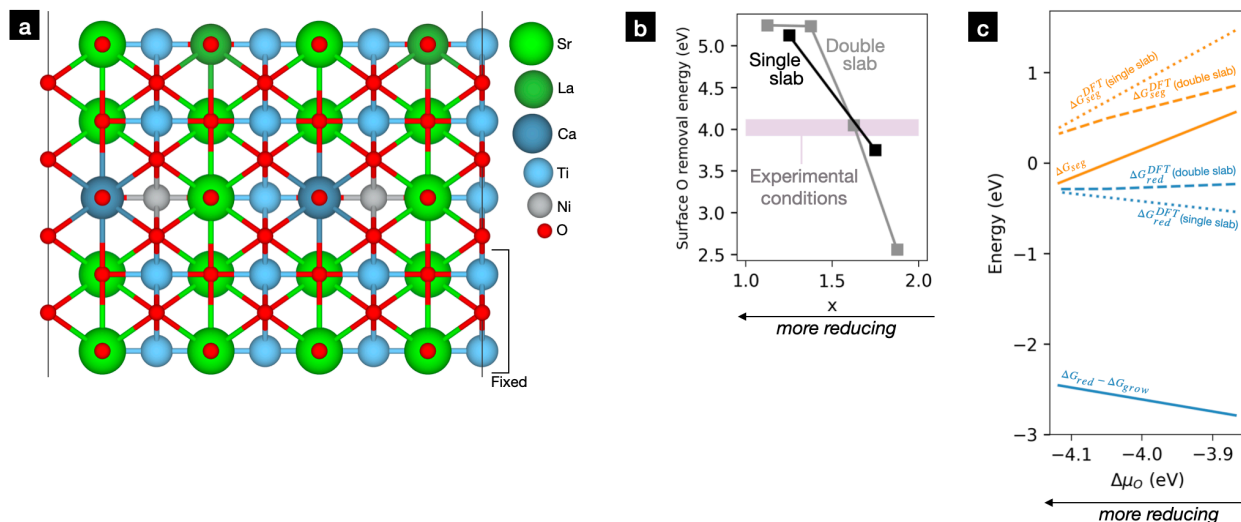


Figure S7. (a) Larger, “double” slab used to calculate O removal energies. (b) Approximate surface O removal energies as a function of x calculated for the “single” (main text) and double slab. Calculated values (points) are in reasonable agreement, but the slopes approximated by linear interpolation differ substantially. (c) Fit segregation and reduction/growth energies of our nucleation model compared to their DFT analogues, calculated using x defined based on the single and double slabs. Calculations using the double slab had substantially different slopes than those based on the single slab.

of this analysis to the size of the DFT model used highlights the need for more accurate treatments of the surface oxygen termination in future work.

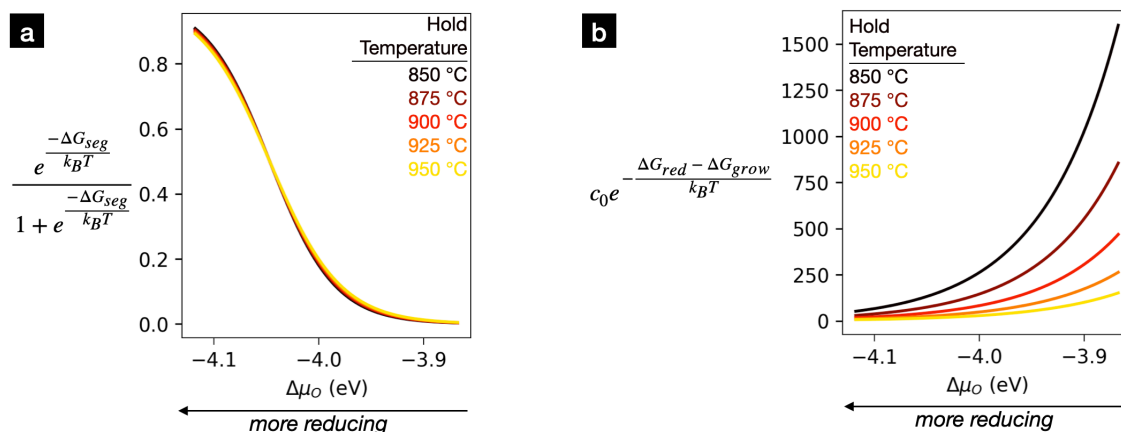


Figure S8. (a) Equilibrium Ni segregation fraction derived from our semiempirical model. Ni segregation thermodynamics become more favorable at more reducing conditions, but were largely unaffected by changes in temperature. (b) Combined Ni-rich surface reduction/nanoparticle growth rate term derived from our semiempirical model. This term shrunk at higher temperatures (likely due to faster growth) and under more reducing conditions (likely a combined effect of a higher Ni reduction barrier and a lower growth rate).

References

- (1) Wu, X.; Yu, Y.; Chen, Y.; Li, L.; Ma, Z.-F.; Yin, Y.-M. Construction of Multifunctional Nanoarchitectures in One Step on a Composite Fuel Catalyst through In Situ Exsolution of $\text{La}_{0.5}\text{Sr}_{0.5}\text{Fe}_{0.8}\text{Ni}_{0.1}\text{Nb}_{0.1}\text{O}_{3-\delta}$. *ACS Appl. Mater. Interfaces* **2020**, *12* (31), 34890–34900. <https://doi.org/10.1021/acsami.0c08016>.
- (2) Lindenthal, L.; Huber, J.; Drexler, H.; Ruh, T.; Rameshan, R.; Schrenk, F.; Löffler, S.; Rameshan, C. In Situ Growth of Exsolved Nanoparticles under Varying rWGS Reaction Conditions—A Catalysis and Near Ambient Pressure-XPS Study. *Catalysts* **2021**, *11* (12), 1484. <https://doi.org/10.3390/catal11121484>.
- (3) Spring, J.; Sediva, E.; Hood, Z. D.; Gonzalez-Rosillo, J. C.; O’Leary, W.; Kim, K. J.; Carrillo, A. J.; Rupp, J. L. M. Toward Controlling Filament Size and Location for Resistive Switches via Nanoparticle Exsolution at Oxide Interfaces. *Small* **2020**, *16* (41), 2003224. <https://doi.org/10.1002/sml.202003224>.
- (4) Tang, C.; Kousi, K.; Neagu, D.; Portolés, J.; Papaioannou, E. I.; Metcalfe, I. S. Towards Efficient Use of Noble Metals via Exsolution Exemplified for CO Oxidation. *Nanoscale* **2019**, *11* (36), 16935–16944. <https://doi.org/10.1039/C9NR05617C>.
- (5) Agüero, F. N.; Beltrán, A. M.; Fernández, M. A.; Cadús, L. E. Surface Nickel Particles Generated by Exsolution from a Perovskite Structure. *J. Solid State Chem.* **2019**, *273*, 75–80. <https://doi.org/10.1016/j.jssc.2019.02.036>.
- (6) Otto, S.-K.; Kousi, K.; Neagu, D.; Bekris, L.; Janek, J.; Metcalfe, I. S. Exsolved Nickel Nanoparticles Acting as Oxygen Storage Reservoirs and Active Sites for Redox CH_4

- Conversion. *ACS Appl. Energy Mater.* **2019**, *2* (10), 7288–7298. <https://doi.org/10.1021/acsaem.9b01267>.
- (7) Kyriakou, V.; Neagu, D.; Zafeiropoulos, G.; Sharma, R. K.; Tang, C.; Kousi, K.; Metcalfe, I. S.; van de Sanden, M. C. M.; Tsampas, M. N. Symmetrical Exsolution of Rh Nanoparticles in Solid Oxide Cells for Efficient Syngas Production from Greenhouse Gases. *ACS Catal.* **2020**, *10* (2), 1278–1288. <https://doi.org/10.1021/acscatal.9b04424>.
- (8) Gao, Y.; Chen, D.; Saccoccio, M.; Lu, Z.; Ciucci, F. From Material Design to Mechanism Study: Nanoscale Ni Exsolution on a Highly Active A-Site Deficient Anode Material for Solid Oxide Fuel Cells. *Nano Energy* **2016**, *27*, 499–508. <https://doi.org/10.1016/j.nanoen.2016.07.013>.
- (9) Shah, S.; Xu, M.; Pan, X.; Gilliard-Abdulaziz, K. L. Exsolution of Embedded Ni–Fe–Co Nanoparticles: Implications for Dry Reforming of Methane. *ACS Appl. Nano Mater.* **2021**, *4* (8), 8626–8636. <https://doi.org/10.1021/acsanm.1c02268>.
- (10) Lai, K.-Y.; Manthiram, A. Evolution of Exsolved Nanoparticles on a Perovskite Oxide Surface during a Redox Process. *Chem. Mater.* **2018**, *30* (8), 2838–2847. <https://doi.org/10.1021/acs.chemmater.8b01029>.
- (11) Kim, J. K.; Jo, Y.-R.; Kim, S.; Koo, B.; Kim, J. H.; Kim, B.-J.; Jung, W. Exceptional Tunability over Size and Density of Spontaneously Formed Nanoparticles via Nucleation Dynamics. *ACS Appl. Mater. Interfaces* **2020**, *12* (21), 24039–24047. <https://doi.org/10.1021/acsaami.0c05215>.
- (12) Schindelin, J.; Arganda-Carreras, I.; Frise, E.; Kaynig, V.; Longair, M.; Pietzsch, T.; Preibisch, S.; Rueden, C.; Saalfeld, S.; Schmid, B.; Tinevez, J.-Y.; White, D. J.; Hartenstein, V.; Eliceiri, K.; Tomancak, P.; Cardona, A. Fiji: An Open-Source Platform for Biological-Image Analysis. *Nat. Methods* **2012**, *9* (7), 676–682. <https://doi.org/10.1038/nmeth.2019>.
- (13) Schneider, C. A.; Rasband, W. S.; Eliceiri, K. W. NIH Image to ImageJ: 25 Years of Image Analysis. *Nat. Methods* **2012**, *9* (7), 671–675. <https://doi.org/10.1038/nmeth.2089>.
- (14) Chase Jr, M. W. NIST-JANAF Thermochemical Tables. *J Phys Chem Ref Data Monogr.* **1998**, *9*.
- (15) Kousi, K.; Neagu, D.; Bekris, L.; Papaioannou, E. I.; Metcalfe, I. S. Endogenous Nanoparticles Strain Perovskite Host Lattice Providing Oxygen Capacity and Driving Oxygen Exchange and CH₄ Conversion to Syngas. *Angew. Chem. Int. Ed.* **2020**, *59* (6), 2510–2519. <https://doi.org/10.1002/anie.201915140>.
- (16) O’Leary, W.; Giordano, L.; Park, J.; Nonnenmann, S. S.; Shao-Horn, Y.; Rupp, J. L. M. Influence of Sr-Site Deficiency, Ca/Ba/La Doping on the Exsolution of Ni from SrTiO₃. *J. Am. Chem. Soc.* **2023**, *145* (25), 13768–13779. <https://doi.org/10.1021/jacs.2c12011>.